50th AIAA Aerospace Sciences Meeting including the New Horizons Forum and Aerospace Exposition, January 9-12, 2012, Nashville, Tennessee

Effects of Riblets on Skin Friction in High-Speed Turbulent Boundary Layers

Lian Duan*
National Institute of Aerospace, Hampton, VA 23666
Meelan M. Choudhari†
NASA Langley Research Center, Hampton, VA 23681

Direct numerical simulations of spatially developing turbulent boundary layers over riblets are conducted to examine the effects of riblets on skin friction at supersonic speeds. Zero-pressure gradient boundary layers with an adiabatic wall, a Mach number of $M_\infty = 2.5$, and a Reynolds number based on momentum thickness of $Re_\theta = 1720$ are considered. Simulations are conducted for boundary-layer flows over a clean surface and symmetric V-groove riblets with nominal spacings of 20 and 40 wall units. The DNS results confirm the few existing experimental observations and show that a drag reduction of approximately 7% is achieved for riblets with proper spacing. The influence of riblets on turbulence statistics is analyzed in detail with an emphasis on identifying the differences, if any, between the drag reduction mechanisms for incompressible and high-speed boundary layers.

Nomenclature

A	surface area, m^2
C_f	Skin friction coefficient
C_p	heat capacity at constant pressure, J/(K·kg)
C_v	heat capacity at constant volume, J/(K·kg)
D	Drag, N
h	riblet height, m
L	Computational domain size, m
M	Mach number, dimensionless
Pr	Prandtl number, $Pr = 0.71$, dimensionless
R	radius of riblet tip
Re_θ	Reynolds number based on momentum thickness and free-stream viscosity, $Re_\theta \equiv \frac{\rho_\infty u_\infty \theta}{\mu_\delta}$, dimensionless
$Re_{\delta 2}$	Reynolds number based on momentum thickness and wall viscosity, $Re_{\delta_2} \equiv \frac{\rho_\infty u_\infty \theta}{\mu_w}$, dimensionless
Re_τ	Reynolds number based on shear velocity and wall viscosity, $Re_\tau \equiv \frac{\rho_w u_\tau \delta}{\mu_w}$, dimensionless
s	riblet spacing, m
T	temperature, K
T_r	recovery temperature, $T_r = T_\infty(1 + 0.9 * \frac{\gamma-1}{2} M_\infty^2)$, K
u	streamwise velocity, m/s
u_τ	friction velocity, m/s
v	spanwise velocity, m/s
w	wall-normal velocity, m/s
z_τ	viscous length, $z_\tau = \nu_w/u_\tau$, m

*Research Scientist. Member, AIAA
†Aerospace Technologist, Computational AeroSciences Branch, M.S. 128. Associate Fellow, AIAA

α riblet ridge angle, $\circ$
γ specific heat ratio, $\gamma = C_p/C_v$, dimensionless
δ boundary layer thickness, m
δ^* displacement thickness, m
θ momentum thickness, m
κ thermal conductivity, $\kappa = \mu C_p/Pr$, W/(m·K)
μ dynamic viscosity, $\mu = 1.458 \times 10^{-6} \frac{T^{3/2}}{T+110.4}$, kg/(m·s)
ν kinematic viscosity, $\nu = \mu/\rho$, m^2·s
ρ density, kg/m^3

Subscripts

f quantities related to flat plate or clean surface
i inflow station for the domain of principal direct numerical simulation
n surface normal direction
r quantities related to riblets
rms root mean sqaure
w wall variables
x streamwise direction of the right-hand Cartesian coordinate
y spanwise direction of the right-hand Cartesian coordinate
z wall-normal direction of the right-hand Cartesian coordinate
∞ freestream variables

Superscripts

$+$ inner wall units
$\overline{(\cdot)}$ averaged variables
$(\cdot)'$ perturbation from averaged variable

I. Introduction

Viscous or skin friction drag accounts for nearly one half of the total drag for a subsonic transport aircraft and one third of the total drag for a supersonic transport aircraft. Over the past two decades, research on skin friction drag reduction has received considerable attention[1,2] and attempts have progressed in two directions: methods for delaying the boundary layer transition and methods for modifying the turbulence structures in a turbulent boundary layer. Among the various passive techniques for controlling turbulent drag, riblets have been extensively investigated, especially for subsonic boundary layers.[3–5] As reviewed by Walsh,[3] consistent drag reductions up to 8% have been achieved via V-groove riblet surfaces at subsonic speeds. By optimizing the riblet geometry, drag reduction of up to 10% has also been reported.[6]

Several mechanisms by which riblets reduce drag have been suggested, including the weakening of the bursting process near the wall,[7] the inhibition or restriction of spanwise motion of longitudinal vortices,[8,9] an increase in sublayer thickness,[8] the significant retardation of the viscous flow in the valley of the riblet groove,[4,10] and the restriction of the location of streamwise vortices above the wetted surface.[11] However, even for a zero-pressure gradient boundary layer flow, the detailed mechanisms are not clearly understood, largely due to the small groove dimensions and the difficulty for measurements in the close vicinity of the grooves.[5]

For supersonic flows, it is reasonable to expect similar effectiveness of riblets as that in the subsonic regime,[2] due to the fact that the microgrooves will be well immersed in the low-speed velocity field, at least for a moderately supersonic Mach number. So far, very limited riblet data at supersonic speeds are available. The few data include wind tunnel investigations at Mach 2.97 by Robinson,[12] Mach 1.5 by Gaudet,[13] Mach 1.6, 2.0, and 2.5 by Coustols and Cousteix,[14] as well as flight tests at Mach 1.2-1.6 by Zuniga et al.[15] These studies report that skin friction drag reduction of up to 15% has been achieved. However, none of the above studies have provided a detailed investigation of the riblet effects on turbulence statistics and the drag reduction mechanisms.

High-fidelity simulations like direct numerical simulations (DNS) and large eddy simulations (LES) provide a vast amount of accurate data that can be used to analyze the interrelationship between riblets and near-wall turbulence and provide necessary information for understanding the mechanism by which riblets reduce drag. For example, Choi et al.,[11] Chu and Karniadakis,[16] and Goldstein et al.[17] conducted DNS of incompressible channel flows with surface-mounted riblets, in which detailed turbulence statistics are pre-

sented and the physical mechanisms that cause drag reduction are hypothesized. More recently, Klumpp et al.[18] performed LES to investigate the influence of an adverse-pressure gradient on the performance of riblets in incompressible turbulent boundary layers. An analysis of riblet effects on drag reduction in the supersonic regime has not been performed and is the target of the present investigation.

In the current paper, we conduct DNS for spatially developing boundary layers in the supersonic regime. Unlike the previous work,[11,16,17] which focused on channel flows, riblets in external flows are examined without any assumption of streamwise periodicity. The effects of riblets on turbulence statistics and large-scale turbulence structures will be addressed. The differences, if any, between the drag reduction mechanisms for incompressible and high-speed boundary layers will be identified.

II. Flow conditions and numerical methodology

The boundary layer edge conditions and wall parameters for the DNS are given in Table 1, which provides freestream Mach number, density, and temperature (M_∞, ρ_∞, and T_∞, respectively) as well as the boundary layer thickness and various Reynolds numbers at the inlet of the domain.

Table 1. Bounday layer edge and wall parameters for the DNS.

M_∞	ρ_∞(kg/m^3)	T_∞(K)	T_w(K)	δ_i(mm)	Re_θ	Re_τ	$Re_{\delta 2}$
2.5	0.1	270.4	568.0	4.58	1719.2	320.7	1006.3

A. Numerical method

To simulate the boundary layer flow over riblets, the compressible Navier-Stokes equations are solved in generalized curvilinear coordinates. The working fluid is assumed to be an ideal gas with a linear (i.e. Newtonian) stress-strain relation. The Fourier law is used to compute the heat flux terms. A 7th order WENO (weighted essentially non-oscillatory) scheme[19] is used to compute the convective flux terms. This particular WENO algorithm combines a high order of accuracy with low dissipation and high bandwidth, which is desirable for time accurate simulations of compressible turbulence. The resolution properties of this scheme are documented in several references.[20,21] For the viscous flux terms, a 4th order central difference scheme is used. The 3rd order low storage Runge-Kutta scheme by Williamson[22] is used for time integration.

B. Boundary conditions

To enable the simulation of a spatially evolving boundary layer, it is important to prescribe the appropriate distribution of flow variables at the inflow boundary. It would be too computationally intensive to conduct a single DNS of the whole flow field, which includes the complete surface where the upstream boundary layer develops, and the downstream region where the boundary layer interacts with surface-mounted riblets. Instead, we conduct an independent auxiliary DNS of a spatially developing boundary layer which provides the inflow boundary condition for the principal DNS over the domain with riblets. In addition, the single auxiliary DNS can be used to provide an identical inflow for the downstream simulations with and without riblets, thus isolating the influence of riblets on skin friction drag. The computational setup for the auxiliary and principal simulations is sketched in Figure 1.

On the wall, no-slip conditions are applied for the three velocity components and an isothermal condition is used for the temperature. The wall temperature is prescribed to be nearly the recovery temperature, as shown in Table 1. At the top and outlet boundaries, unsteady non-reflecting boundary conditions based on Thompson[23] are imposed. Periodic boundary conditions are used in the spanwise direction.

C. Flow configuration and computational mesh

The computational setup for the auxiliary and principal simulations is sketched in Figure 1. The domain for the auxiliary DNS measures approximately $10.9\delta_i$ in the streamwise direction, $2.8\delta_i$ in the spanwise direction,

and $9.8\delta_i$ in the wall-normal direction, with $320\times129\times121$ grid points in the streamwise, spanwise, and wall-normal directions, respectively. Uniform grid spacings are used in the streamwise and spanwise directions, with $\Delta x^+ = 10.4$ and $\Delta y^+ = 6.8$. Geometrically stretched grids are used in the wall-normal direction with $\Delta z^+ = 0.3$ at the wall. The grid characteristics for the auxiliary DNS are consistent with those reported in the literature in the context of previous simulations of turbulent wall bounded flows using comparable numerical algorithms.[24–27] At the inlet of the auxiliary DNS, the rescaling boundary condition of Xu & Martín[28] is used, with the recycling station located approximately $8\delta_i$ downstream of the inlet. It is also at this position that the flow slice is temporally sampled and spatially interpolated to provide the inlet boundary condition for the principal DNS with riblets. A similar approach has been successfully applied by Priebe & Martín[29] to provide the inflow for the study of shock wave and turbulent boundary layer interaction.

For the principal DNS, three sets of simulations with different surface topologies have been performed. The first is a clean-surface baseline simulation (denoted as M25Clean), and the other two include riblets with nominal riblet spacings of $s^+ \approx 20$ and $s^+ \approx 40$, respectively (denoted as M25s20 and M25s40). Triangular riblets with ridge angle 45° are used for both M25s20 and M25s40 (Figure 2b). The case of smaller riblet spacing corresponds to a drag-reducing configuration and the larger spacing case corresponds to a drag-increasing configuration. Similar riblet topologies have been explored in the experiments of Walsh[30] and DNS of Choi et al.[11] under incompressible conditions. For cases M25s20 and M25s40, the riblets begin at a distance $x \approx 0.4\delta_i$ downstream of the inlet of the principal DNS, while upstream of this position the surface remains clean to gurantee a nearly unperturbed flow at the inlet. Moreover, the grids consist of a smooth streamwise transition from the clean surface to the riblet surface to minimize the extent of upstream/downstream influence due the surface variation. The streamwise length for the transitional zone is approximately 4 times that of the riblet height h with the grid streamwise refined, as is shown in Figure 2a. The streamwise grid becomes unifrom past the transitional zone. The riblet zone has a streamwise length of approximately $7.7\delta_i$ with a resolution of approximately $\Delta x^+ = 10.5$ in the streamwise direction. The spanwise grids are clustered near the riblet tips and coarsened near riblets valleys, with 32 grid points on the surface of each riblet. To improve smoothness of the grids and avoid singularities when evaluating the Jacobian, the periodic riblet geometry with sharp corners has been approximated by a truncated Fourier series expansion containing the first six terms. The Fourier filtering gives slightly rounded riblet tips and valleys with radius $R/s \approx 4\%$. The extent of rounding is within a range where no significant degradation in riblet performances is expected.[31,32] Moreover, the investigation of flow over rounded riblets is of practical relevance since it is hard to precisely machine a riblet surface which assumes sharp peaks, and the tips of riblets mounted on an aircraft fusalage or wing can undergo deterioration as often as every flight operation.[16] A close-up view of riblet geometry and near-wall grids has been sketched in Figure 2b. 20 and 10 riblets are used for M25s20 and M25s40, respectively, which corresponds to a spanwise domain of approximately 440 wall units.

Table 2 outlines the domain sizes and grid resolutions for Cases M25s20 and M25s40. The smallest values of Δy^+_{min} and Δz^+_{min} occur near the riblet tip and the larger values occur near the riblet valley. The clean surface case has similar domain sizes and grid resolution as the case M25s20 for comparison purposes.

Table 2. Simulation parameters for the direct numerical simulations of turbulent flows over riblets. The value of Δx corresponds to that in the uniform region (outsize of the transitional zone). 20 and 10 riblets are used for M25s20 and M25s40, respectively, with 32 points for each riblet.

Case	s^+	h^+	L_x/δ_i	L_y/δ_i	L_z/δ_i	Δx^+	Δy^+_{min}	Δz^+_{min}	$N_x \times N_y \times N_z$
M25Clean	NA	NA	8.7	1.4	9.8	10.8	0.28–1.05	0.28	$256 \times 640 \times 120$
M25s20	21.4	10.4	8.2	1.4	9.8	10.4	0.27–1.02	0.20–0.27	$256 \times 640 \times 120$
M25s40	45.3	22.0	8.4	1.4	9.8	11.1	0.67–2.14	0.13–0.28	$256 \times 320 \times 120$

Both the domain size and the grid resolution exceed those used by Choi et al.[11] for the riblet simulations, despite the higher order scheme used in the present study. For instance, the domain sizes in the streamwise/spanwise directions for the current riblets simulations ($L_x^+ \times L_y^+ \approx 2600 \times 440$) are significantly

larger than those used by Choi et al.[11] ($L_x^+ \times L_y^+ \approx 570 \times 160$). In addition, to further investigate the dependence of viscous drag on spanwise domain size and grid resolution, two test runs have been carried out for the case M25s20, one with the same grid resolution as case M25s20 but half the spanwise width (10 riblets or $L_y^+ \approx 220$), and the other with the same spanwise width but double the grid resolution (64 grid points per riblet). The differences in skin friction drag between the case M25s20 and either test run are within 1.0%. Moreover, the DNS results over flat plates have been compared with existing experimental and well-established numerical data.[24] In particular, Figure 3 shows good agreement between the current DNS and that by Guarini et al.[33] at Mach 2.5 and $Re_\theta = 1570$.

III. Results

In this section, we examine the effects of riblets on skin-friction drag and other turbulence statistics. Statistics are collected near a streamwise location $x_a \approx 7\delta_i$, which is significantly downstream of the beginning of the riblet surface to avoid any significant effects due to surface transition. To obtain statistics, averages are first calculated over a streamwise window of $[x_a - 0.6\delta_i, x_a + 0.6\delta_i]$ and the same spanwise locations over different riblets for each instantaneous flow field; then, an ensemble average over flow field snapshots spanning a time interval of more than $150\delta_i/u_\infty$ is calculated. Reducing the number of flow fields for the ensemble averaging by one third results in less than 0.5% difference in viscous drag. We use an overbar to indicate an averaged quantity and a prime to indicate perturbations from this average. The origin of the z coordinate corresponds to the wall location for clean surfaces. For cases with riblets, the riblets are mounted on top of the otherwise clean surface with $z = 0$ corresponding to the riblet valley. This computational setup mimics the practical applications that riblets are molded into a lightweight plastic film with an adhesive backing and pressed into place on the surface of a vehicle.

A. Drag measurement

The total skin-friction drag, D, is obtained as the integral of the product of the wall shear stress and the differential wetted area

$$D = \int_{A_r} \mu_w \left(\frac{\partial u}{\partial n}\right)_w dA_r = \tau_w^* A_f = \mu_w \left(\frac{\partial u}{\partial n}\right)_f^* A_f \tag{1}$$

where A_r denotes the wetted area of a riblet surface and $A_f = A_r cos(\alpha) = L_x \times L_y$ is its corresponding clean-surface area (see Figure 4).

The skin friction coefficient, C_f, is defined as

$$C_f = \frac{\overline{\tau}_w^*}{\frac{1}{2}\rho_\infty u_\infty^2} \tag{2}$$

and the wall-shear velocity u_τ^* and viscous length z_τ^* for riblet surface are defined as

$$u_\tau^* = \sqrt{\frac{\overline{\tau}_w^*}{\overline{\rho}_w}}\ , \qquad z_\tau^* = \frac{\overline{\mu}_w}{\overline{\rho}_w u_\tau^*}\ . \tag{3}$$

The superscript $*$ has been added to u_τ and z_τ to emphasize their relevance to the global riblet surface and distinguish them from the local values at a particular spanwise location.

Figure 5 shows the time history of plane-averaged wall-shear rate $\left(\frac{\partial u}{\partial n}\right)_f^*$ (defined by Equation 1) for various cases. Relative to the clean surface, the drag reduction for M25s20 and the drag increase for M25s40 are clearly seen. Table 3 further shows the time-averaged skin friction and the drag variation relative to the clean surface for the two riblet cases. Drag is reduced by approximately 7% for the $s^+ \approx 20$ case and increased by approximately 4% for the $s^+ \approx 40$ case. The drag reduction for the smaller riblet-spacing case confirms the observations of the few existing experiments under supersonic conditions.[13–15] The drag variations are also similar to several incompressible results. For comparison, with similar riblet geometries, the experiments by Walsh[30] report a drag reduction of 2% for $s^+ \approx 20$ and drag increase of 3% for $s^+ \approx 40$, and the DNS by Choi et al.[11] give drag reduction of 5% for $s^+ \approx 20$ and drag increase of 2% for $s^+ \approx 40$.

To distinguish the different contributions from riblet tips and valleys to the total drag, Figure 6 plots the wall-shear rate as a function of spanwise position along the riblet. It is seen that, at both conditions,

the wall shear rate at riblet tips is significantly higher than the flat-plate value, while the wall shear rate at riblet valleys is well below the flat-plate value. Whether riblets reduce or increase drag depends on whether the reduction in the riblet valleys is sufficient to overcome the skin-friction increase near riblet tips. Compared with M25s40, the $s^+ \approx 20$ case has relatively smaller wall shear throughout most spanwise locations, consistent with the smaller total drag, but it actually has slightly higher wall shear at the tip.

Table 3. Area averaged skin friction C_f, friction velocity u_τ^*, and viscous length $z^*\tau$ for M25s20 and M25s40. In the second column, + and − denote the drag increase and decrease, respectively, relative to the smooth wall.

Case	$C_f \times 10^3$	$\frac{(C_f)_{riblet}-(C_f)_{smooth}}{(C_f)_{smooth}}$	u_τ^*/u_∞	z_τ^*/δ_i
M25s20	2.331	−7.0%	0.0493	0.00327
M25s40	2.616	+4.4%	0.0523	0.00309

B. Virtual origin

In this Section, we introduce the concept of virtual origin to account for the surface geometry conditions and facilitate the comparison of boundary-layer profiles among various surface topologies.

The virtual origin of a riblet surface is defined as the location z_0 of an imaginary flat surface which has the same drag as the riblet surface and matches the riblet velocity profile above the viscous sublayer. The use of virtual origin can be justified by the lack of spanwise variations in the streamwise velocity above certain z-location, as shown by the streamwise velocity contour in the transverse plane (Figure 7). The spanwise variation in the velocity occurs only near the riblets and there is no apparent variations of mean velocity in the spanwise direction above $z^+ = 50$. Similar observations have also been reported for incompressible flows by multiple researchers.[11,34,35]

Several methods of evaluating the virtual origin have been proposed by multiple researchers.[8,9,11,34] For example, Bechert and Bartenwerfer[9] evaluated the virtual origin based on the variation in the mean velocity and obtained

$$z_0 = z_{mid} + \beta s \tag{4}$$

where z_{mid} is the midpoint between the riblet tip and valley, and β is a constant depending only on the ridge angle ($\beta = 0.11$ for V-groove riblets with ridge angle of 45°). Choi et al.[11] evaluated the virtual origin based on the wall-normal shift in the location of maximum turbulent kinetic energy production (or the maximum intensity of the streamwise velocity fluctuation), and proposed

$$z_0 = \frac{(z_{mr}^+ - z_{mf}^+)\nu_w}{u_\tau^*} \tag{5}$$

where z_{mr} and z_{mf} are the locations of maximum turbulent kinetic energy production (or the maximum streamwise velocity fluctuation intensity) for riblet and flat surfaces, respectively. This definition is considered more reliable because it takes into account the combined influence of riblet geometry and the flow parameters.

Table 4 outlines the locations of virtual origins based on Equation 5 for the two riblet cases. The difference in β between M25s20 and M25s40 indicates that the virtual origin is not only a function of the ridge angle as predicted by Equation 4, but also depends on the riblet spacing. As a result, Equation 5 will be used in the rest of the paper to calculate the location of virtual origin.

The effects of virtual origin can be demonstrated by comparing the mean velocity profiles plotted with and without the introduction of virtual origin. Figure 8a shows that riblets push the mean location of the no-slip surface further into the flow, and such displacement increases with riblet height. After the introduction of the virtual origin, the mean velocity profiles largely overlap except very close to the riblets, as shown by Figure 8b.

Table 4. Location of virtual origin for each riblet configuration. Note, $z = 0$ corresponds to the riblet valley. The virtual origin z_0 is calculated following Equation 5 with $z_{mf} = 12.5$. $z^+_{tip} = (z_{tip} - z_0)u^*_\tau/\nu_w$, and β is computed from Equation 4 given z_0.

Case	z^+_0	z^+_{tip}	β
M25s20	7.7	2.7	0.117
M25s40	17.0	5.0	0.132

C. Turbulence statistics

Turbulence statistics are plotted using the virtual origin calculated above to take into account the shift in the mean location of the no-slip surface due to riblets, as $z^+ = (z - z_0)/z^*_\tau$. The turbulence statistics are normalized either by the freestream quantities to demonstrate the changes in absolute magnitude, or by the wall units to investigate the structural variations in near-wall turbulence characteristics.

Figures 9a, 9c, and 9e show that all three components of turbulence intensity for M25s20 decrease relative to the clean surface case, consistent with the reduction in C_f for this case. For M25s40, much stronger spanwise variations are found because of the larger penetration of riblets into the boundary layer. The peak values above the tip are larger than those of the clean surface while the peak values above the valley are smaller, which is consistent with spanwise variation in the wall-shear rate (Figure 6) and the consequent overall increase in the viscous drag. The introduction of virtual origin largely accounts for the upward shift in profiles due to riblets. When normalized using u^*_τ, which takes into account the drag variation, a much better collapse with the clean-surface profiles is achieved for M25s20, as show in in Figures 9b, 9d, and 9f. For M25s40, however, the collapse in profiles with the clean-surface profile is not as good as that of M25s20. The Reynolds shear stress, shown in Figure 10, demonstrates a similar trend to turbulent intensities for both riblet cases.

The changes in turbulence intensities and Reynolds shear stress are consistent with the experimental observation by Robinson[12] at Mach 2.97 and are similar to several incompressible results.[11,17]

D. Near-wall turbulence structures and drag reduction mechanisms

Figure 11b and Figure 11d plot cross-flow velocity vectors (v,w) and contours of the streamwise vorticity component in the transverse plane for Cases M25s20 and M25s40, respectively. For the drag-reducing configuration (M25s20), Figure 11b shows that most streamwise vortical structures are limited by the small riblet spacing and, hence, stay above the riblets. As a result, only a limited area near the riblet tips is exposed to the downwash of high-speed fluid induced by these vortical structures and the high shear rates (red contours) are consequently restricted to the tips, as indicated by Figure 11a. For the drag-increasing configuration, however, Figure 11d shows that the streamwise vortical structures are able to penetrate further into the valleys of the riblets and a larger area is exposed to the high-speed downwash, resulting in a larger region of high shear rates (Figure 11c). Similar observations have been reported by Choi[11] while investigating incompressible channel flows over riblets, conforming that the dynamics of riblet flows is not significantly modified by compressibility effects up to a Mach number of 2.5.

IV. Conclusions

This paper presented direct numerical simulations of turbulent boundary layers over riblets at a supersonic Mach number. The DNS results show that drag reduction of approximately 7% is achieved for riblets with proper spacing, similar to the drag reduction measured in the few existing experiments at supersonic Mach numbers. In addition, the DNS results show that the effects of riblets on turbulence statistics and large-scale structures closely resemble those at low speeds. In particular, riblets damp turbulence intensities and Reynolds shear stress near the wall for the drag-reducing configuration. The flow visualizations of near-wall structures seem to support the hypothesis of Choi et al.[11] that riblets with small spacing reduce viscous

drag by restricting the location of streamwise vortices above the wetted surface so that only a limited area is exposed to the downwash of high-speed fluid induced by these streamwise vortices.

The DNS results provide evidence that the effectiveness of riblets would prevail under supersonic speeds, at least up to a moderate Mach number, although further investigations for a broader set of flow parameters and riblet geometries are still necessary to establish the dependence of drag reduction on Mach number, wall cooling, and Reynolds number.

Acknowledgments

This work was performed as part of the Supersonics Project of NASA's Fundamental Aeronautics Program (FAP). The authors would like to thank Prof. Pino Martín of the University of Maryland for providing the original code used in this effort.

References

[1]Bushnell, D. M. and McGinley, C. B., "Turbulence Control in Wall Flows," *Annual Review of Fluid Mechanics*, Vol. 21, No. 1, Jan. 1989, pp. 1–20.

[2]Bushnell, D. M., "Viscous Drag Reduction in Aeronautics," *Proceedings of the 19th Congress International Council Aeronautical Science*, Anaheim, CA, 1994.

[3]Walsh, M. J., "Riblets," *Progress in Astronautics and Aeronautics*, Washington, DC, AIAA, 1990, pp. 203–261.

[4]Coustols, E., "Riblets: Main Known and Unknown Features," *In: K. S. Choi, K. K. Prasad, T. V. Truong, editors. Emerging Techniques in Drag Reduction. Mechanical Engineering Publications, UK*, 1996, pp. 3–43.

[5]Viswanath, P. R., "Aircraft Viscous Drag Reduction Using Riblets," *Progress in Aerospace Sciences*, Vol. 38, No. 6-7, Aug. 2002, pp. 571–600.

[6]Bechert, D. W., Bruse, M., Hage, W., Hoeven, J., and Hoppe, G., "Experiments on Drag-Reducing Surfaces and Their Optimization with an Adjustable Geometry," *Journal of Fluid Mechanics*, Vol. 338, 1997, pp. 59–87.

[7]Schwarz-van, M., Thijssen, J., Nieuwvett, C., Prasad, K., and Nieuwstadt, F., "The Bursting Process over Drag Reducing Grooved Surfaces," *Proceedings of the IUTAM Symposium on Structure of Turbulence and Drag Reduction*, Berlin, Springer, 1990, pp. 561–568.

[8]Choi, K., "Near-Wall Structure of a Turbulent Boundary Layer with Riblets," *Journal of Fluid Mechanics*, Vol. 208, 1989, pp. 417–458.

[9]Bechert, D. W. and Bartenwerfer, M., "The Viscous Flow on Surfaces with Longitudinal Ribs," *Journal of Fluid Mechanics*, Vol. 206, 1989, pp. 105–129.

[10]Suzuki, Y. and Kasagi, N., "Turbulent Drag Reduction Mechanism above a Riblet Surface," *AIAA Journal*, Vol. 32, No. 9, sep 1994, pp. 1781–1790.

[11]Choi, H., Moin, P., and Kim, J., "Direct Numerical Simulation of Turbulent Flow over Riblets," *Journal of Fluid Mechanics*, Vol. 255, 1993, pp. 503–539.

[12]Robinson, S. K., "Effects of Riblets on Turbulence in a Supersonic Boundary Layer," AIAA Paper 88-2526, 1988.

[13]Gaudet, L., "Properties of Riblets at Supersonic Speed," *Applied Scientific Research*, Vol. 46, No. 3, July 1989, pp. 245–254.

[14]Coustols, E. and Cousteix, J., "Performances of Riblets in the Supersonic Regime," *AIAA Journal*, Vol. 32, No. 2, 1994, pp. 431–433.

[15]Zuniga, F. A., Anderson, B. T., and Bertelrud, A., "Flight Test Results of Riblets at Supersonic Speeds," NASA Technical Paper 4387, 1992.

[16]Chu, D. C. and Karniadakis, G. E., "A Direct Numerical Simulation of Laminar and Turbulent Flow over Riblet-Mounted Surfaces," *Journal of Fluid Mechanics*, Vol. 250, 1993, pp. 1–42.

[17]Goldstein, D., Handler, R., and Sirovich, L., "Direct Numerical Simulation of Turbulent Flow over a Modelled Riblet Covered Surface," *Journal of Fluid Mechanics*, Vol. 302, 1995, pp. 333–376.

[18]Klumpp, S., Guldner, T., Meinke, M., and Schröder, W., "Riblets in a turbulent adverse-pressure gradient boundary layer," AIAA Paper 2010-4585, 2010.

[19]Jiang, G. and Shu, C., "Efficient Implementation of Weighted ENO Schemes," *Journal of Computational Physics*, Vol. 126, No. 1, June 1996, pp. 202–228.

[20]Martín, M. P., Taylor, E. M., Wu, M., and Weirs, V. G., "A Bandwidth-Optimized WENO Scheme for the Direct Numerical Simulation of Compressible Turbulence," *Journal of Computational Physics*, Vol. 220, No. 1, 2006, pp. 270–289.

[21]Taylor, E. M., Wu, M., and Martín, M. P., "Optimization of nonlinear error sources for weighted non-oscillatory methods in direct numerical simulations of compressible turbulence," *Journal of Computational Physics*, Vol. 223, 2006, pp. 384–397.

[22]Williamson, J., "Low-Storage Runge-Kutta Schemes," *Journal of Computational Physics*, Vol. 35, No. 1, 1980, pp. 48–56.

[23]Thompson, K. W., "Time Dependent Boundary Conditions for Hyperbolic Systems," *Journal of Computational Physics*, Vol. 68, No. 1, Jan. 1987, pp. 1–24.

[24]Martín, M., "DNS of Hypersonic Turbulent Boundary Layers. Part I: Initialization and Comparison with Experiments," *Journal of Fluid Mechanics*, Vol. 570, 2007, pp. 347–364.

[25]Duan, L., Beekman, I., and Martín, M. P., "Direct Numerical Simulation of Hypersonic Turbulent Boundary Layers. Part 3: Effect of Mach Number," *Journal of Fluid Mechanics*, Vol. 672, 2011, pp. 245–267.

[26]Duan, L., Beekman, I., and Martín, M. P., "Direct Numerical Simulation of Hypersonic Turbulent Boundary Layers. Part 2: Effect of Wall Temperature," *Journal of Fluid Mechanics*, Vol. 655, 2010, pp. 419–445.

[27]Duan, L. and Martín, M. P., "Direct Numerical Simulation of Hypersonic Turbulent Boundary Layers. Part 4: Effect of High Enthalpy," *Journal of Fluid Mechanics*, Vol. 684, 2011, pp. 25–59.

[28]Xu, S. and Martín, M. P., "Assessment of Inflow Boundary Conditions for Compressible Turbulent Boundary Layers," *Physics of Fluids*, Vol. 16, No. 7, 2004, pp. 2623–2639.

[29]Priebe, S. and Martín, M. P., "Analysis of Low-Frequency Unsteadiness in the Direct Numerical Simulation of a Shockwave and Turbulent Boundary Layer Interaction," AIAA Paper 2009-3711, 2009.

[30]Walsh, M. J., "Turbulent Boundary Layer Drag Reduction Using Riblets," AIAA Paper 82-0169, 1982.

[31]Walsh, M. J. and Lindemann, A. M., "Optimization and Application of Riblets for Turbulent Drag Reduction," AIAA Paper 84-0347, 1984.

[32]Walsh, M. J., "Effect of Detailed Surface Geometry on Riblet Drag Reduction Performance," *Journal of aircraft*, Vol. 27, No. 6, 1990, pp. 572–573.

[33]Guarini, S. E., Moser, R. D., Shariff, K., and Wray, A., "Direct Numerical Simulation of a Supersonic Turbulent Boundary Layer at Mach 2.5," *Journal of Fluid Mech.*, Vol. 414, 2000, pp. 1–33.

[34]Hooshmand, A., Wallace, R. A., Wallace, J. M., and Balint, J. L., "An Experimental Study of Changes in the Structure of a Turbulent Boundary Layer due to Surface Geometry Changes," AIAA Paper 83-0230, 1983.

[35]Benhalilou, M., Anselmet, F., Liandrat, J., and Fulachier, L., "Experimental and Numerical Investigation of a Turbulent Boundary Layer over Riblets," *Proceedings of the 8th Symposium on Turbulent Shear Flows*, September 9-11, Technical University of Munich, 1991, pp. 18.5.1–18.5.6.

[36]Robert, J. P., "Drag Reduction: An Industrial Challenge," *AGARD-R-796*, March 1992.

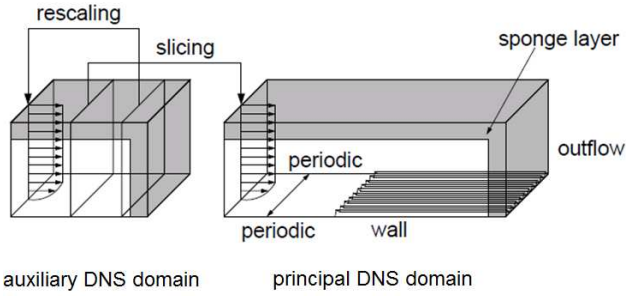

Figure 1. Sketch of DNS domain for spatial simulations (modified from Klumpp[18])

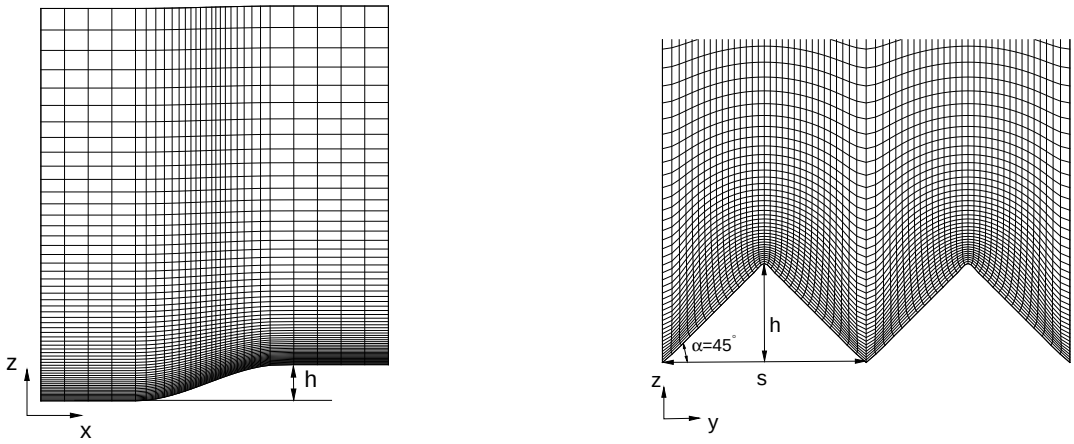

(a) Side view of the transition from clean surface to riblets

(b) Close-up view of riblet configuration

Figure 2. Computational mesh near riblets for M25s20.

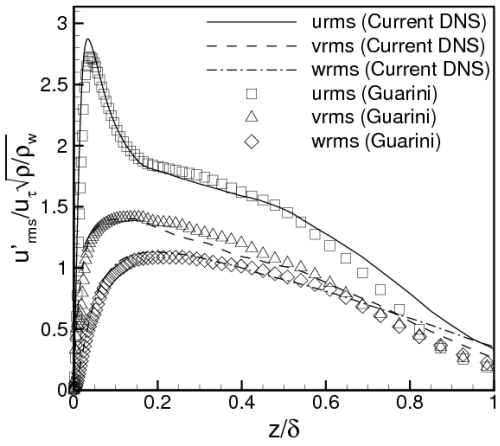

Figure 3. RMS of velocity components compared with the DNS by Guarini et al.[33]

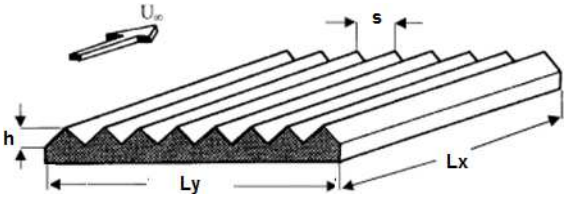

Figure 4. Sketch of riblet geometry (modified from Robert[36])

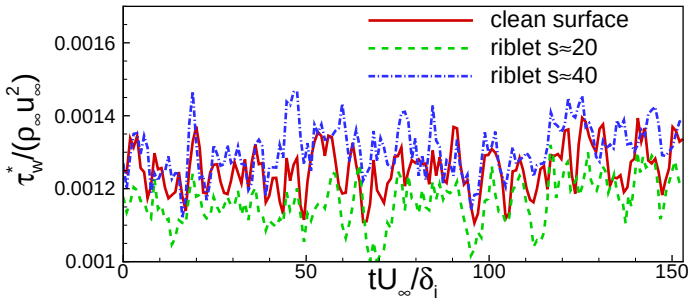

Figure 5. Time history of wall-shear rates for various Mach 2.5 cases.

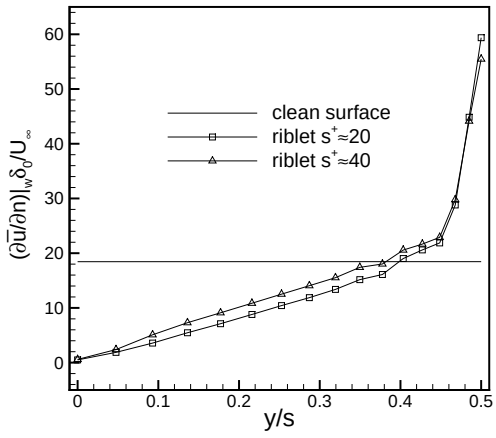

Figure 6. Wall-shear rates at various spanwise positions on riblet surface for Mach 2.5 cases.

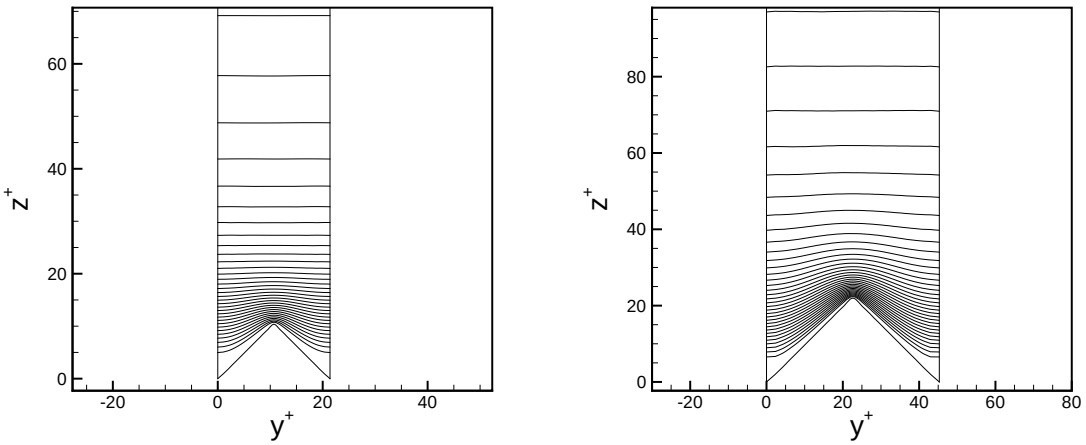

(a) M25s20 **(b) M25s40**

Figure 7. Contours of the mean streamwise velocity in the (y, z) plane. The contour levels normalized by u_∞ range from 0.05 to 0.95 by increments of 0.0225.

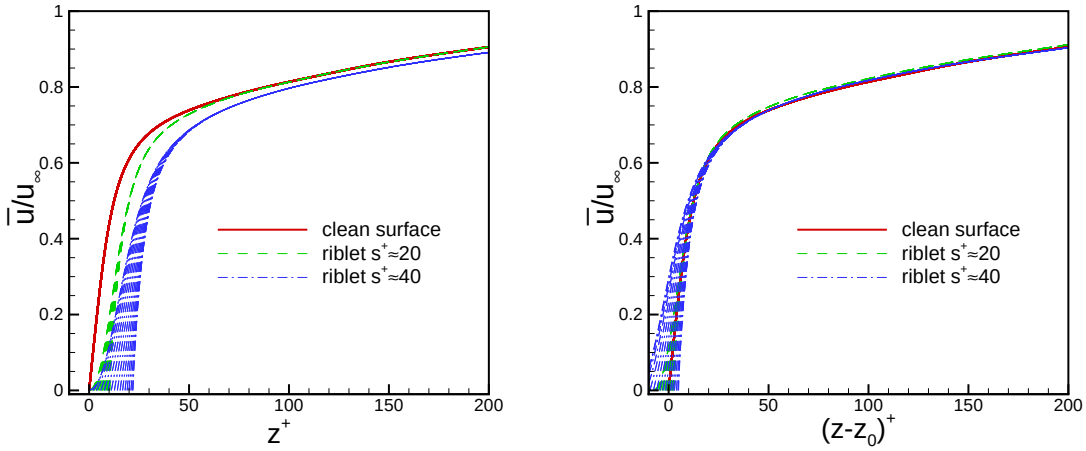

(a) Without offset

(b) Offset by virtual origin

Figure 8. Mean streamwise velocity profiles near riblets without and with offset by virtual origin. The virtual origin is defined by Equation 5.

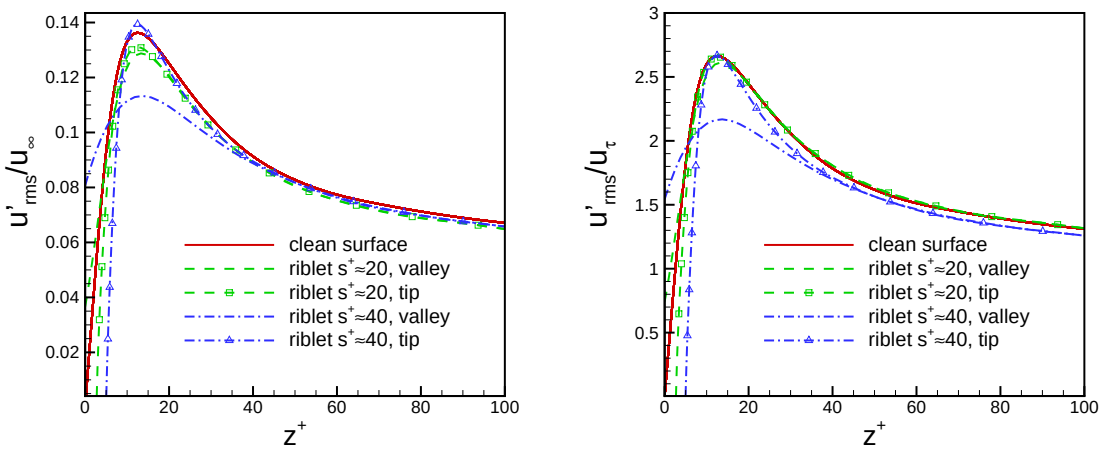

(a) Streamwise

(b) Streamwise

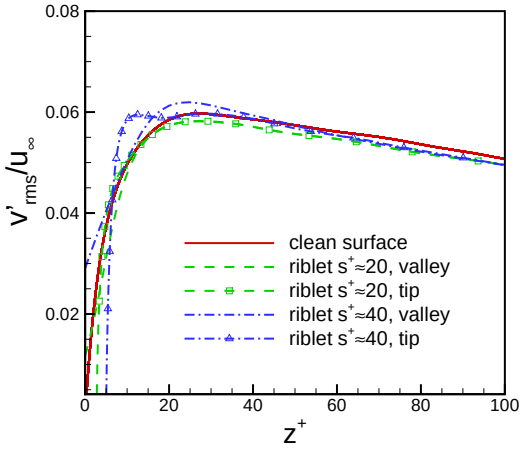

(c) Spanwise

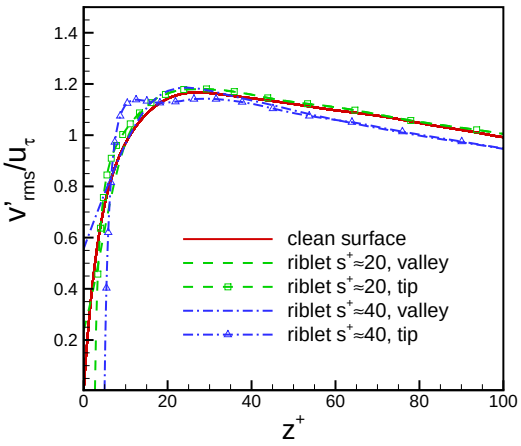

(d) Spanwise

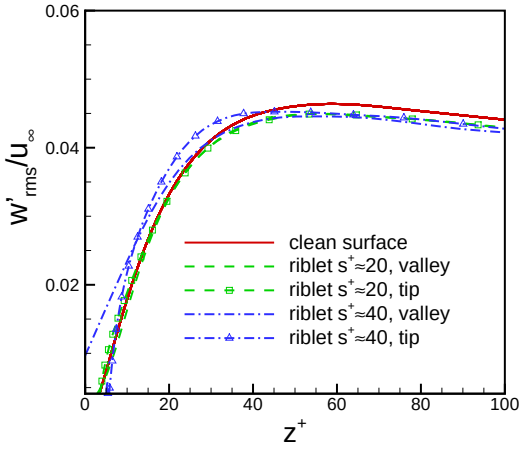

(e) Wall normal

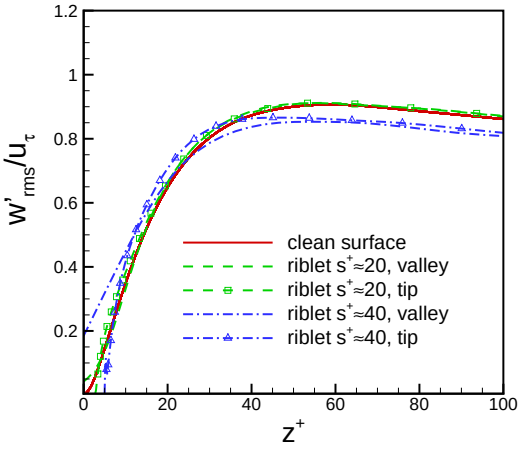

(f) Wall normal

Figure 9. Turbulence intensities normalized by freestream velocity u_∞ (Left) or friction velocity u_τ^* (Right).

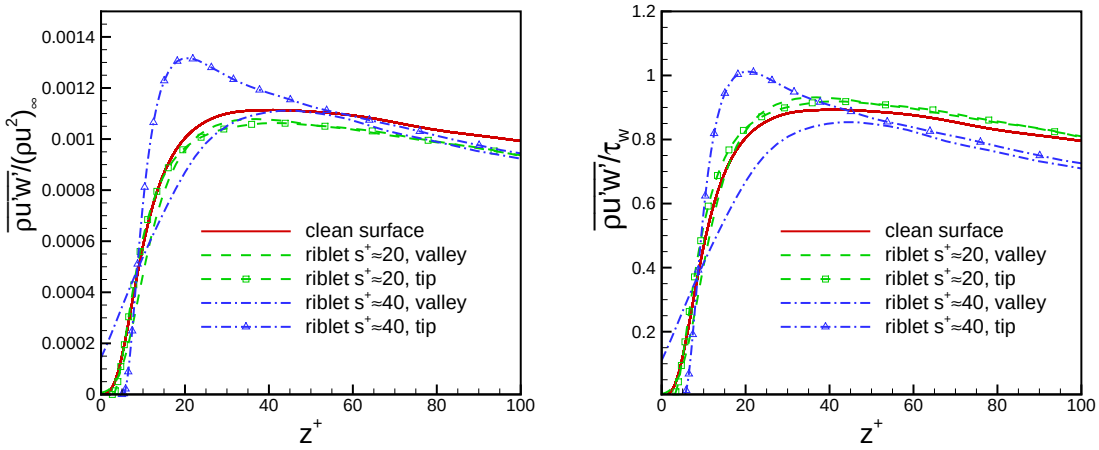

(a) (b)

Figure 10. Reynolds shear stress normalized by freestream or wall quantities.

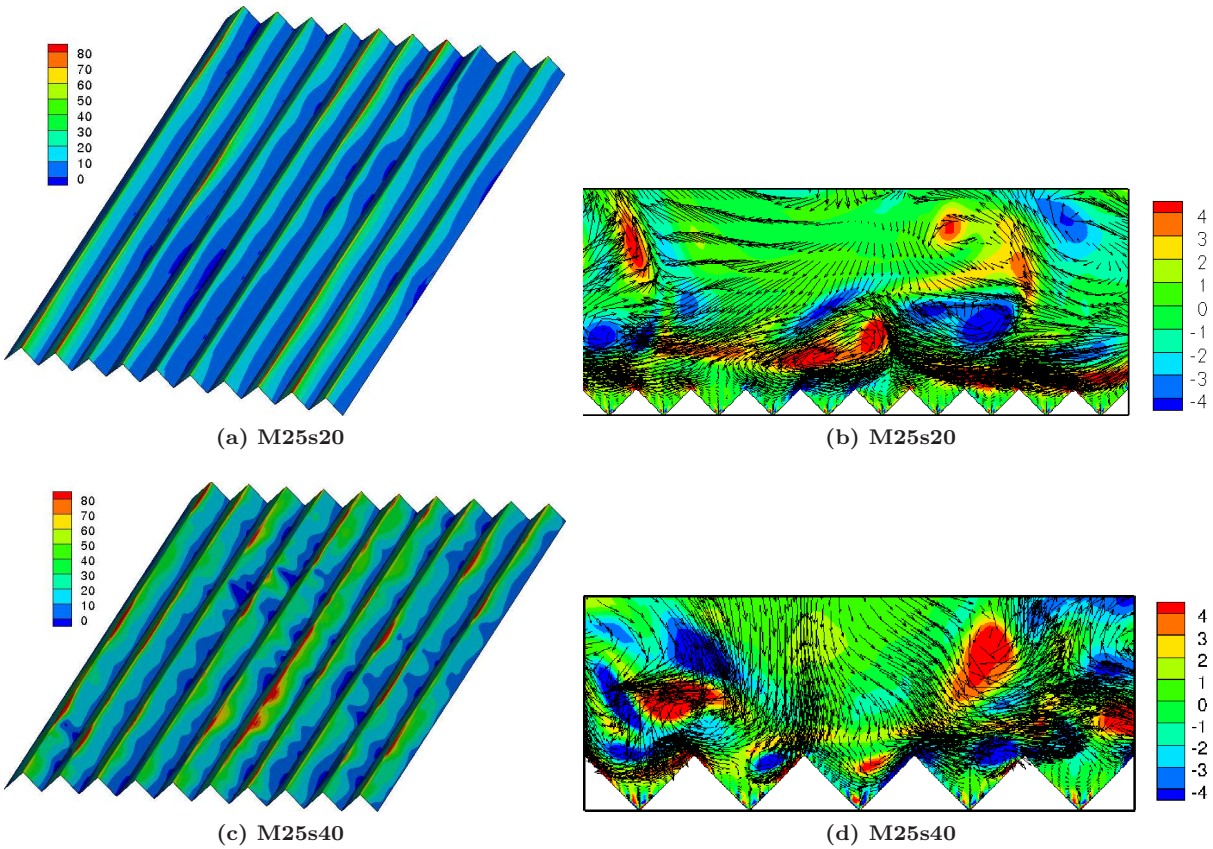

(a) M25s20 (b) M25s20

(c) M25s40 (d) M25s40

Figure 11. Instantaneous flows over riblets: (*a*,*c*) contours of the wall-shear rate on the riblet surfaces; (*b*,*d*) cross-flow velocity vectors (v, w) and contours of the streamwise vorticity in the (y,z)-plane.